

From Micro to Large Scale Models: Porosity Homogenization Schemes for DEM Simulations

Moris Kalderon¹, M.Sc., DIC
National Technical University of Athens

Edward Smith, Ph.D.
Brunel University London

C. O’Sullivan, Ph.D.
Imperial College London

ABSTRACT

There are many applications where require in-depth understanding of the underlying dynamics of the fluid-particle interaction and predict phenomena which are detrimental for human lives. For example, internal erosion in dams and beneath flood embankments can be occurred due to the variation in the total head of the fluid causing particle motion, slope instabilities can be triggered due to fluid flows and liquefaction can be caused from an increase in the fluid pressure. All these failures are triggered by actions at a micro-scale, constituting the coupled CFD-DEM models the optimum numerical tool in the hands of an engineer; DEM is used to resolve the soil as particles and CFD is applied for the depiction of the fluid phases. A critical issue on DEM-CFD simulations is the selection of a suitable homogenization coarse graining scheme, in other words a method to translate particulate mechanics into continuum mechanics. Within this contribution two novel porosity coarse-graining strategies are proposed including a Voxel method where a secondary dense grid of “pixel-cells” is implemented adopting a binary logic for the coarse graining and a Hybrid method where both analytical formulas and pixels are utilized. The proposed methods are compared with four porosity coarse-graining schemes that have been documented in the literature, including the Particle Centroid Method (PCM), an Analytical method, a method which solves the diffusion equation and an approach which employs averaging using kernels. A detailed comparison is then presented for all six schemes considering “accuracy”, “smoothness” and “computational cost”. Optimal parameters are obtained for all six methods and recommendations for coarse graining DEM samples are discussed.

Keywords: coarse graining, DEM, porosity, homogenization

INTRODUCTION

There are many reasons why one might want to upscale, homogenize or Coarse-Grain (CG), the particle information available from a Discrete Element Method (DEM) simulation to obtain a continuum field. For instance, to predict the liquefaction-induced settlements and the corresponding structural damages of the superstructure (Bullock et al., 2019; Forcellini, 2020; Xue & Yang, 2014) or study improvement methods to reduce the liquefaction potential of sands subjected to a shaking (Lopez-Caballero & Modaressi-Farahmand-Razavi, 2013). Also, reasons may include the assessment of internal erosion in dams and beneath flood embankments due to the variation in the total head of the fluid, as well as scour and sand production in oil reservoirs (Foster et al., 2000; O’Sullivan, 2011). These include a desire to interpret the simulation data within

¹ Moris Kalderon, MSc., DIC, *National Technical University of Athens*, moriska@mail.ntua.gr

the continuum mechanics framework in which much of our understanding of material behaviour has evolved, the need to upscale data for use in multi-scale modelling approaches or where a DEM code is coupled with a Computational Fluid Dynamics (CFD) solver. This last application, coupling DEM-CFD simulations, is the motivation for this study. Specifically, this contribution is relevant to the unresolved coupling approach where the fluid is modelled at a scale much larger than individual particles, so the particle information is treated in an average manner.

There are many CG methods documented in the literature such as the Particle centroid method (PCM) (Hoomans et al., 1996; Kawaguchi et al., 2000; Tsuji et al., 1993), Approximate methods (Darmana et al., 2005; Khawaja et al., 2012; Tomiyama et al., 1997; Wu et al., 2009), the Particle meshing method (PPM) (Peng et al., 2016), Satellite point methods, (Boyce et al., 2014; Clarke et al., 2018; Fitzgerald et al., 2019; Mema et al., 2019), Exact methods (Bnà et al., 2015; Freireich et al., 2010; Strobl et al., 2016; Wu et al., 2009), Porous particle methods (PPM) (Jing et al., 2016; Kloss et al., 2012; Link et al., 2005), Statistical kernel methods (Glasser & Goldhirsch, 2001; Goldhirsch, 2010; Imole et al., 2016; Roy et al., 2019; Xiao & Sun, 2011; Zhu & Yu, 2002), Diffusion based methods (Sun & Xiao, 2015a, 2015b) etc. In the current study, six CG algorithms are assessed (Kalderon et al., 2021). These are *the Particle centroid method (PCM)*, an *Analytical method*, a *Diffusion-based*, a *Kernel-based method* together with two new approaches, the *Voxel-based method* and the *Hybrid method*. The averaging algorithms are initially presented both in two and three dimensions. Then, the calibration process and the results of the prior tests are illustrated, followed by a comparison in terms of accuracy, smoothness and computational cost. Finally, the advantages of the proposed Voxel and Hybrid methods are provided in the concluding section.

METHODOLOGY

Any coarse-graining algorithm must consider particles moving freely in a specific domain, so that their centroid can be located at any random position within each Eulerian cell. Four different cases can be identified. In Category A particles are completely contained within the cell; in this case the whole area / volume of the particle is attributed to the specific cell. Category B considers the particles that intercept the boundary between two cells and as a result the particles are divided into two segments. For Category C the particles overlap the intersection of 4 (2D) or 8 (3D) Eulerian cells. The fourth category refers to the case where particles intersect the external boundaries of the sample (Category D). The applications considered in this study used periodic boundaries, consequently the portion of the particle located outside the sample boundaries is essentially attributed to the opposite Eulerian cell. Hereinafter, the proposed CG schemes are described and are mathematically formulated, together with versions of the most widely used CG schemes found in literature.

Implemented Schemes

Particle Centroid Method (PCM): This is the simplest but crudest approach to obtain a porosity coarse-grained field. The whole particle area is attributed to the cell containing the particle's centroid even when the particle extends beyond the cell boundaries. The porosity of a Eulerian cell using the PCM is as follows:

$$n = \frac{V_{cell} - \sum_{i=1}^{N_p} V_i^p}{V_{cell}} \quad (1)$$

where V_{cell} is the volume of the Eulerian cell, V_i^p is the volume of particle i and N_p is the number of particles contributing to the cell considered.

Analytical method: This method calculates the exact overlap volume (or area in 2D) of a particle and a cuboid bin by integrating the sphere's (or circle's in 2D) equation. Referring to **Figure 1** the integral limits are defined as the intersection of the planes defining the bin boundaries and the particle. This method assumes that the smallest dimension of the bin is larger than the circle's diameter and the implication of this assumption is that a 2D particle (circle) can be in contact with at most two mutually perpendicular bin walls or planes and a sphere with at most three. The mathematical formulations used are based on Strobl et al. (2016), Richards (1995) and Freireich et al. (2010). In two dimensions the overlapping area A_{cap} is calculated from Equation (2) and the segment A_4 by Equation (3):

$$A_{cap} = r_p^2 \cos^{-1} \left(\frac{r_p - h}{r_p} \right) - (r_p - h) \sqrt{2r_p h - h^2} \quad (2)$$

$$A_4 = \int_{L_1}^{L_2} \left(\left(\sqrt{r_p^2 - (x - x_c)^2} \right) + y_c \right) dx \quad (3)$$

where r_p is the particle radius, h is the disk segment height, x_c, y_c are the particle centroid coordinates and L_1, L_2 are the limits of the integral along the x - axis. The remaining segments are calculated by simple subtractions and the portions are allocated to the corresponding bins.

The first step to estimate each partial volume is to calculate the total sphere volume and the spherical cap volume, see Equation. Next the volumes due to edge overlap and corner overlap are determined according to Equations (4), (5), (6). Finally, after all the portions are known the volumes are allocated to the relevant bin.

$$V_{cap} = \frac{1}{3} \pi h^2 (3r_p - h) \quad (4)$$

$$V_{edge} = \frac{2}{3} ab \sqrt{r_p^2 - a^2 - b^2} + 2r_p^3 \tan^{-1} \left(\frac{b \sqrt{r_p^2 - a^2 - b^2}}{r_p a} \right) + \frac{2}{3} r_p^3 \tan^{-1} \left(\frac{a \sqrt{r_p^2 - a^2 - b^2}}{r_p b} \right) - \frac{1}{3} (3br_p^2 - b^3) \tan^{-1} \left(\frac{\sqrt{r_p^2 - a^2 - b^2}}{a} \right) - \frac{1}{3} (3ar_p^3 - a^3) \tan^{-1} \left(\frac{\sqrt{r_p^2 - a^2 - b^2}}{b} \right) \quad (5)$$

$$V_{corner} = V_{segm.7} = \frac{1}{2} V_{edge} - \frac{1}{6} \left[6abc - 2ac \sqrt{r_p^2 - a^2 - c^2} - 2bc \sqrt{r_p^2 - b^2 - c^2} - (3ar_p^2 - a^3) \tan^{-1} \left(\frac{c}{\sqrt{r_p^2 - a^2 - c^2}} \right) + 2r_p^3 \tan^{-1} \left(\frac{bc}{r_p \sqrt{r_p^2 - b^2 - c^2}} \right) + (c^3 - 3cr_p^2) \tan^{-1} \left(\frac{b}{\sqrt{r_p^2 - b^2 - c^2}} \right) - (3br_p^2 - b^3) \tan^{-1} \left(\frac{c}{\sqrt{r_p^2 - b^2 - c^2}} \right) + 2r_p^3 \tan^{-1} \left(\frac{ac}{r_p \sqrt{r_p^2 - a^2 - c^2}} \right) + (3cr_p^2 - c^3) \tan^{-1} \left(\frac{\sqrt{r_p^2 - a^2 - c^2}}{a} \right) \right] \quad (6)$$

where r_p is the particle radius and a, b, c are the distances between the particle centroid and the corresponding bin face. The detailed descriptions of each scenario and the derivation of the equations are presented in Kalderon (2017).

Kernel method: This method is based on the generation of a Eulerian field, from multiplication of particle positions by a weighting, generated using a Gaussian or Lucy function, so the particle density is distributed or “smoothed” over the support of the weighting function. Porosity is calculated indirectly and a heuristic approach is taken to explain the procedure. The volume fraction can be calculated in arbitrary positions on the sample’s domain as a summation of the particles’ distributed volumes included in the zone of influence of the kernel. Here, a Gaussian kernel is allocated to each particle and porosity of each Eulerian cell is estimated based on the contribution of each particle volume. Consequently, the smeared volume is a function of the

distance between the particle and the Eulerian cell, as well as the shape of the kernel. **Figure 1b** shows schematically the process that porosity of Eulerian cell $(i, j + 1)$ is calculated. The contribution of particles 1, 2, 3 to the volume fraction ($V_{i,j+1}^{cell}$) depends on the distance (r) between the particle and the cell centroid, which should be less than the kernel's bandwidth (b_k) ($r_k \leq b_k$). The contribution of a particle to a cell is given by Equation (7) for the 2D case and Equation (8) for the 3D case, assuming a Gaussian kernel in both cases.

$$V_i^{cell,k} = \frac{V_i^p}{\pi b^2} e^{-\frac{(x-x_{c,k})^T(x-x_{c,k})}{b^2}} \quad (7)$$

$$V_i^{cell,k} = \frac{V_i^p}{(\pi b^2)^{3/2}} e^{-\frac{(x-x_{c,k})^T(x-x_{c,k})}{b^2}} \quad (8)$$

where, $V_i^{cell,k}$ is the volume "contributed" by particle k to Eulerian cell i , V_i^p is the volume of particle k , b is the kernel bandwidth, \mathbf{x} a vector of the Eulerian cells coordinates and $\mathbf{x}_{c,k}$ a vector of particle coordinates.

Diffusion based method: This method was established to smooth the porosity CG field that is produced by the PCM method and increase accuracy. Porosity essentially is redistributed by solving the diffusion equation with initial conditions being the Eulerian cell porosity values derived from the PCM. The initial conditions correspond to time t , where porosity redistribution has not occurred yet and the final conditions correspond to time $t + \Delta t$, i.e after diffusion is completed, see **Figure 1c**. Time is introduced to describe a pseudo-timestep between the initial and final conditions and is used only to solve diffusion equation.

$$\frac{\partial n(r, t)}{\partial t} = D \nabla^2 n(\mathbf{x}, t) \quad (9)$$

Where, n is the diffused quantity at location \mathbf{x} and time t and D is the diffusion coefficient. The numerical finite difference method is adopted to solve the diffusion equation, hence in 2D dimensions for $\Delta x = \Delta y = \Delta s$ and $a = 2D \frac{\Delta t}{\Delta s^2}$ we have:

$$n_{i,j}^{t+\Delta t} = a(n_{i+1,j}^t + n_{i-1,j}^t + n_{i,j+1}^t + n_{i,j-1}^t - 4n_{i,j}^t) + n_{i,j}^t \quad (10)$$

Similarly, in three dimensions for $\Delta x = \Delta y = \Delta z = \Delta s$ and $a = D \frac{\Delta t}{\Delta s^2}$ the solution is:

$$n_{i,j,k}^{t+\Delta t} = a(n_{i+1,j,k}^t + n_{i-1,j,k}^t + n_{i,j+1,k}^t + n_{i,j-1,k}^t + n_{i,j,k+1}^t + n_{i,j,k-1}^t - 6n_{i,j,k}^t) + n_{i,j,k}^t \quad (11)$$

The diffusion coefficient a describes the rate of diffusion and is used to in place of the constants D , Δt and ΔS , which have no physical meaning here. Selecting a suitable value for coefficient a is the main challenge associated with using this approach.

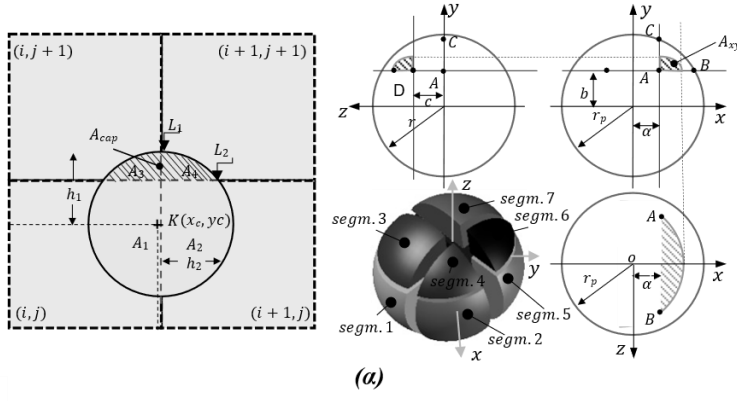
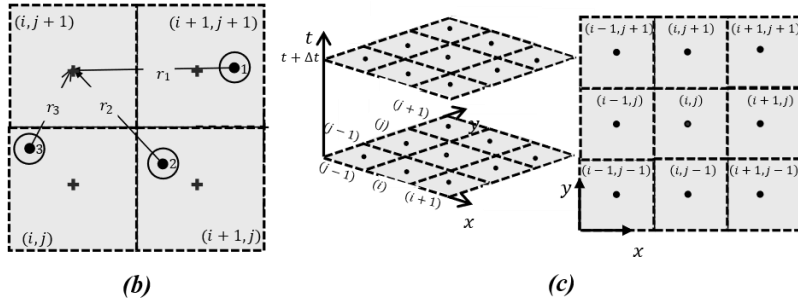


Figure 1. (a) (left) Indicative segment segregation and depiction of the integration limits in the Analytical method (left) 2D and (right) 3D. (b) Illustration of distributed volumes in Kernel method. (c) Schematic explanation of diffusion process.



Proposed schemes

Voxel method: The Voxel method was developed in the current study as an alternative to the Analytical method. The algorithm is based on the discretization of the whole sample domain introducing a dense secondary grid of small regular “pixel” cells. The density of the grid can be user-defined to control the resolution so that accuracy increases as the voxel size reduces. Two loops are used to scan the 2D sample in both horizontal and vertical direction in order to define the location of each voxel in respect to the particle's location. Similarly, in 3D samples the same procedure is applied with an additional loop to cover the extra dimension. Voxels that are covered by particles (particle voxels) are assigned with one and those which are covered by fluid (fluid voxels) are assigned with zero. The application of this method requires the secondary mesh to be few times smaller than the mean particle diameter. **Figure 2a** illustrates with ex and cross symbols the voxel cells centroids of the Eulerian cell $(i+1, j+1)$, where crosses denote the fluid voxels and exes the Particle voxels. In other words, a binary logic is applied to determine whether a specific voxel centroid is covered by a particle. The distance of each voxel to the nearest cell corner is then calculated and the volume of the particle voxel is added to the corresponding Eulerian cell.

Hybrid method: The Hybrid method can be considered as a special case of the Voxel method, where the Analytical method is employed for trivial calculations. Specifically, the area/volume of the particles is calculated analytically only when the circle/sphere overlaps one cell face or is entirely inside one Eulerian cell. Otherwise, when the sphere overlaps more than two cell faces, and the analytical approach becomes more complex, the calculation is achieved by pixel/voxel summation. In two dimensions the area of the circular particle is approximated by applying a second dense square grid extending one diameter from the particle's centre and the area is calculated by summing the area of the boxes that are shaped between the grid lines and are located within the circle's area. Similarly, in three dimensions the volume of the spherical particle is approximated by applying a cuboid grid and the volume is calculated by summing the volume of the corresponding boxes. An example of the method is described in **Figure 2b**, where the volume of particle voxel 1 is allocated in Eulerian cell $(i, j+1)$, the volume of particle voxel 2 in Eulerian cell $(i+1, j+1)$, the volume of particle voxel 3 in Eulerian cell (i, j) and the volume of particle voxel 4 in Eulerian cell $(i+1, j)$.

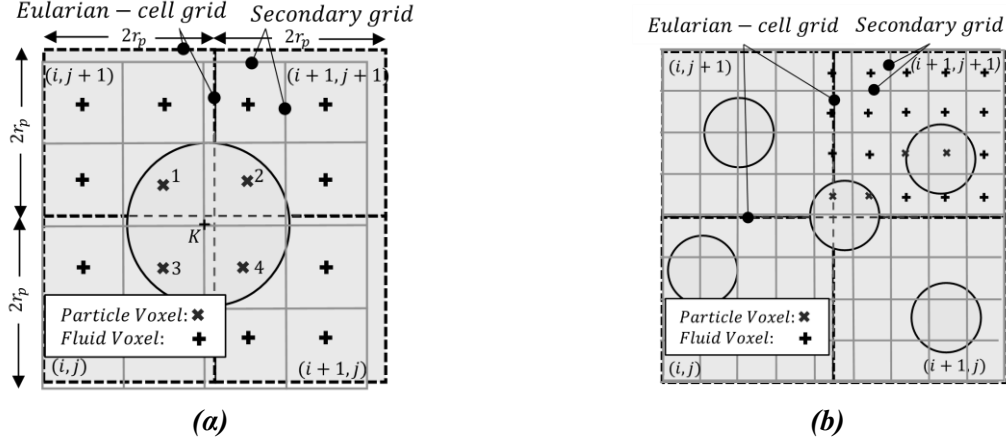


Figure 2. (a) Depiction of Voxel method double grid. The voxels that their centre is located in the particle area are counted and then allocated to the corresponding bins. (b) Schematic of Hybrid method function when the particle is intercepted by more than two fluid cells.

A PRIORY CALIBRATION OF THE ALGORITHMS

In order to fairly compare the methods, the optimal performance of each method must be determined by tuning the parameters such as voxel size, kernel bandwidth or diffusion coefficient. This can be thought of as a calibration of the various methods to ensure a fair comparison and achieve accuracy, smoothness, and computational cost. Computational cost is determined by implementation of all the methods in MATLAB® (2010), an interpreted language which allows us to focus on just algorithmic cost with no compiler optimization. Naturally, some bias may be introduced by the author as the algorithms have not been extensively optimized, however all approaches have been implemented using the same programming language and operating system.

The accuracy of the results of each implementation is judged relative to the Analytical method, which calculates the exact fraction of each sphere inside a cubic cell. The relative error between the two porosity fields is defined as follows:

$$Error (\%) = \frac{1}{No_{Eulerian-cells}} \sum_{i=1}^{No_{cells}} \frac{|n_{cell,i}^{examined} - n_{cell,i}^{analytical}|}{n_{cell,i}^{analytical}} * 100 \quad (12)$$

where $n_{cell,i}^{examined}$ is the porosity value of the Eulerian cell i calculated by the examined method, $n_{cell,i}^{analytical}$ is the porosity value of the Eulerian cell i calculated by the Analytical method (reference method) and $No_{Eulerian-cells}$ is the total number of cells considered in the sample.

As stated in the introduction achieving a “smooth” averaged field from the DEM is an important factor to achieve a numerically stable CFD simulation. Smoothness is measured as the gradient of porosity between the adjacent cells as follows:

$$smoothness = \frac{1}{No_{cells}} \sum_{i=1}^{No_{cells}} \nabla n(\mathbf{x})_i \quad (13)$$

where $\mathbf{x} = x, y$ in two dimensions and $\mathbf{x} = x, y, z$ in three dimensions. The computational cost is assessed as the CPU time required to obtain the porosity field for an identical system run on the same computer with timing obtained as the average of several repeats.

The Kernel, Diffusion, Voxel and Hybrid methods have user-specified parameters which determine how well they perform based on competing accuracy, smoothness, and computational cost considerations. For the Kernel methods this is the adjustable bandwidth “ b ”, while the Diffusion method has diffusivity coefficient included in the parameter α , see Equation (11). Similarly, the number of pixels can be varied in the Voxel and Hybrid methods along with the number of Eulerian cells selected for the sample. According to this calibration process

the number of Eulerian cells is studied indirectly and is defined as $No_{Eulerian-cells} = \left(\frac{Sample\ size}{X*2r_p^{max}}\right)^d$, where r_p^{max} is the largest particle radius, *Sample size* is the width of the Sample (square or cubic samples are considered), d is the number of dimensions (2D versus 3D) and X is a multiplier that controls the size of the cells. To this end, the $No_{Eulerian-cells}$ is different for each sample but the multiplier X allows us to directly compare samples of different size. A multiplier X greater than 1 is proposed in order to avoid Eulerian cells fully occupied by particles, therefore the following five multipliers were adopted in this study: $X = 2$, $X = 3$, $X = 4$, $X = 5$ and $X = 6$.

The 2D schemes were calibrated based on five samples of disks generated by Summersgill (2009) using the two-dimensional DEM code, PFC-2D (Itasca Consulting Group Inc., 2008). The prescribed analysis density was $\rho=2600\text{kg/m}^3$, while the rest of the parameters are summarized in **Table 1**.

Table 1. Summary of the 2D samples simulation parameters

Sample	Maximum number of discs	Distribution for Disc generation	Maximum radius (m)	Wall length (m)	Disc Friction Coefficient
<i>10000gr12p5fb0a</i>	10000	Gaussian	2.5	500	0
<i>10000gr15fb1b</i>	10000	Gaussian	5	1000	1
<i>10000gr120fb0a</i>	10000	Gaussian	20	4000	0
<i>10000ur15fb0b</i>	10000	Uniform	5	850	0
<i>100000gr15fb0p5b</i>	100000	Gaussian	5	3300	0.5

The 3D DEM data were generated using a modified version of LAMMPS (Plimpton, 1995) by Shire (Shire, 2014). The eight cubic samples were created within periodic boundaries and the Hertz-Mindlin contact model was adopted. The simulation parameters are Poisson ratio $\nu=0.3$, shear modulus $G=27\text{GPa}$ and particle density $\rho=2670\text{kg/m}^3$.

Table 2 summarizes the simulation of parameters of the linearly samples and **Table 3** summarizes the simulation of parameters of the bimodal samples. Pictures of the two and three dimensional samples are provided in **Figure 3**.

Table 2. Summary of the 3D linearly graded samples simulation parameters.

Sample	Coefficient of uniformity (Cu)	Interparticle friction coefficient (μ)	Sample characterization	Number of particles	Average particle radius (m)	Wall length (m)
<i>L1.2a</i>	1.2	0	Dense	8262	0.000117	0.00223
<i>L1.2b</i>	1.2	0.1	Medium	8262	0.000117	0.00223
<i>L1.2c</i>	1.2	0.3	Loose	8262	0.000117	0.00223
<i>L3a</i>	3	0	Dense	22600	0.000148	0.0049
<i>L3b</i>	3	0.1	Medium	22600	0.000148	0.0049
<i>L3c</i>	3	0.3	Loose	22600	0.000148	0.0049
<i>L6a</i>	6	0	Dense	59183	0.00015	0.0076
<i>L6b</i>	6	0.1	Medium	59183	0.00015	0.0076
<i>L6c</i>	6	0.3	Loose	59183	0.00015	0.0076

Table 3. Summary of the 3D bimodal samples simulation parameters.

Sample	Size ratio, d_{coarse}/d_{fine}	Fines content, $F_{fine}(\%)$	Number of particles	Average particle radius (m)	Wall length (m)
<i>B2a</i>	2	20	307	0.000666	0.0046
<i>B2b</i>	2	25	367	0.000636	0.0047
<i>B2c</i>	2	30	443	0.000613	0.0048
<i>B2d</i>	2	35	531	0.000594	0.0049
<i>B6a</i>	6	20	5588	0.000182	0.0043
<i>B10a</i>	10	20	25376	0.000103	0.0043

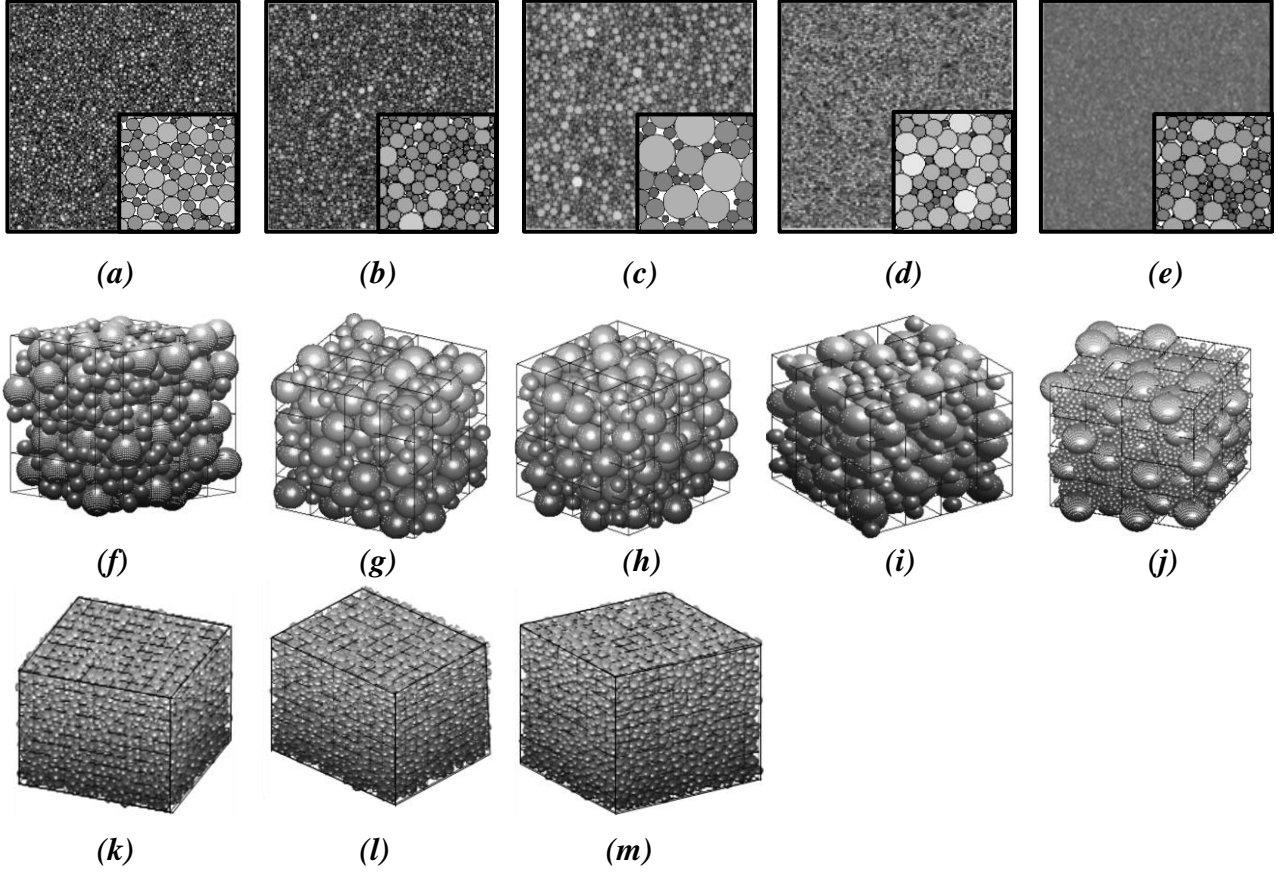


Figure 3. Images of the samples considered for the calibration: (a) 10000gr12p5fb0a, (b) 10000gr15fb1b, (c) 10000gr120fb0a, (d) 10000ur15fb0b, (e) 100000gr15fb0p5b (f) B2a, (g) B2b, (h) B2c, (i) B2d. (j) B6a, (k) L1.2a, (l) L1.2b, (m) L1.2c.

Figure 4 gives an estimation of the accuracy and computational time of the *Voxel* and *Hybrid* methods as an average of the studied samples for Eulerian cell size multipliers from $X=2$ to 6. In other words, every sample is tested for different number of Eulerian cells and accuracy is depicted as the average error of these tests, whilst the maximum and minimum deviation is presented with error bars. A fitting curve is added to provide an estimation of the expected error, where P_i is the number of Pixels along each direction of the sample, $P_i = \sqrt[2]{Pixels}$ in 2D and $P_i = \sqrt[3]{Pixels}$ in 3D.

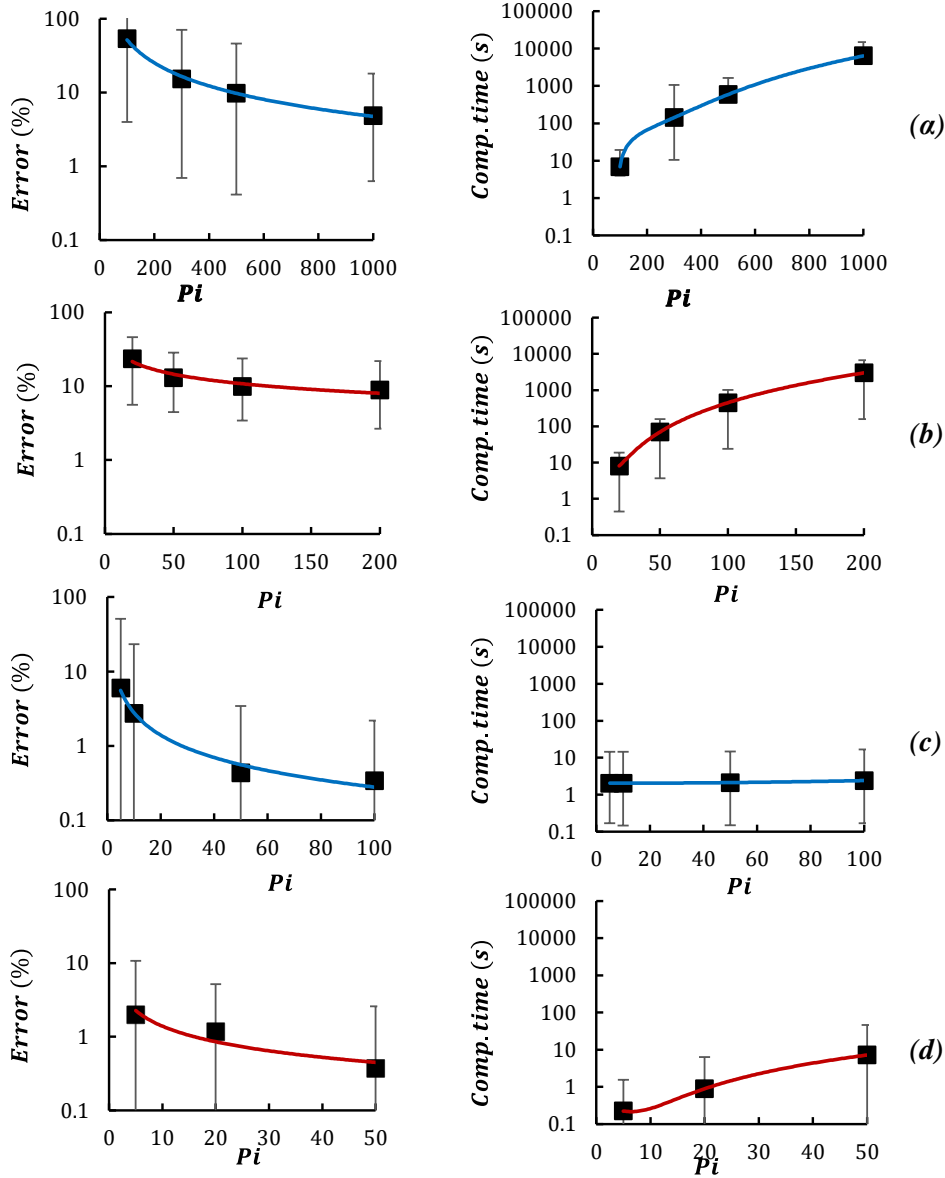


Figure 4. Calibration of (a) 2D Voxel method (b) 3D Voxel method (c) 2D Hybrid method (d) 3D Hybrid method. (left) Error (%) vs Number of Pi , (right) Computational time vs Number of Pi .

As far as the *Voxel method* is concerned a parametric investigation is conducted for four (4) different resolutions. These are $Pi = 100$, $Pi = 300$, $Pi = 500$ and $Pi = 1000$ in the 2D samples and $Pi = 20$, $Pi = 50$, $Pi = 100$ and $Pi = 200$ in the 3D samples. **Figure 4a** shows that when the resolution is low, for example $Pi = 100$ the average error is 53%, although the computational time is just 6 sec. On the other hand, when resolution is increased to $Pi = 300$ or $Pi = 500$ the average error reduces to 15% and 10%, respectively. Unfortunately, the computational cost increases approximately two order of magnitude compared to the low-resolution case, reaching 140 sec. for $Pi = 300$ and 590 sec. for $Pi = 500$. In case of the 3D samples, see **Figure 4b**, porosity CG field cannot be accurately represented by the lowest resolution ($Pi = 20$, average error=24%), although it looks appealing due to the tolerable computational time (8 sec.). Here, the target is to keep a balance between accuracy and computational time. Thus, a resolution of $Pi = 300$ for the 2D samples and $Pi = 50$ for the 3D samples is suggested.

The performance of *Hybrid method* in two dimensions is assessed for the four (4) resolutions depicted in **Figure 5**. From visual observation, it is apparent that when the coarse grid is utilized only a crude approximation of the particle is obtained, while a more accurate representation of the particle shape is available when more than $Pi = 50$ is used. The 3D *Hybrid method* is studied for $Pi = 5$, $Pi = 20$ and $Pi = 50$, see **Figure 4d**. When resolution increases from $Pi=5$ to $Pi=20$ the average error reduces from 2% to 1.2 %, while for a higher resolution, i.e. $Pi=50$ the error is estimated 0.4%, yet the computational time is one order of magnitude higher than before. Consequently, a resolution of $Pi=50$ is considered the most suitable selection for the 2D samples and $Pi=20$ for the 3D samples.

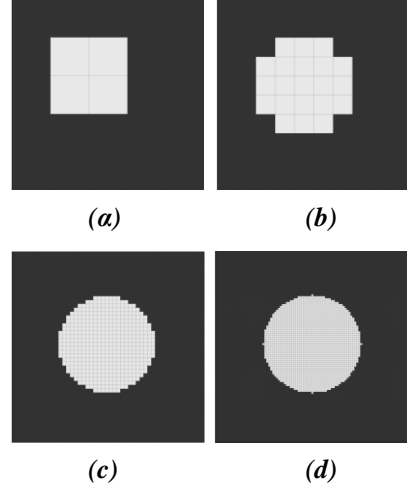


Figure 5. Illustration of particle images produced by the Hybrid method for resolution (a) $Pi = 5$ (5x5 pixels), (b) $Pi = 10$ (10x10 pixels), (c) $Pi = 50$ (50x50 pixels) (d) $Pi = 100$ (100x100 pixels).

Next, the selection of a suitable bandwidth (b) for the *Kernel method* is examined by introducing a normalized bandwidth ($b/\Delta s$), where $\Delta s = X * 2r_p^{max}$. Accuracy, which is translated to minimum error compared to the *Analytical method*, is the optimisation criterion, as computational time is not affected by the kernel size. Specifically, the optimization algorithm seeks the normalized bandwidth value with minimum error, ignoring any local minima, for each X , which as was stated previously, controls the size of the cells. **Figure 6a** illustrates the optimum $b/\Delta s$ values with the X multiplier for (left) the 2D and (right) 3D method, revealing that the bandwidth size can be correlated with the size of the Eulerian cell.

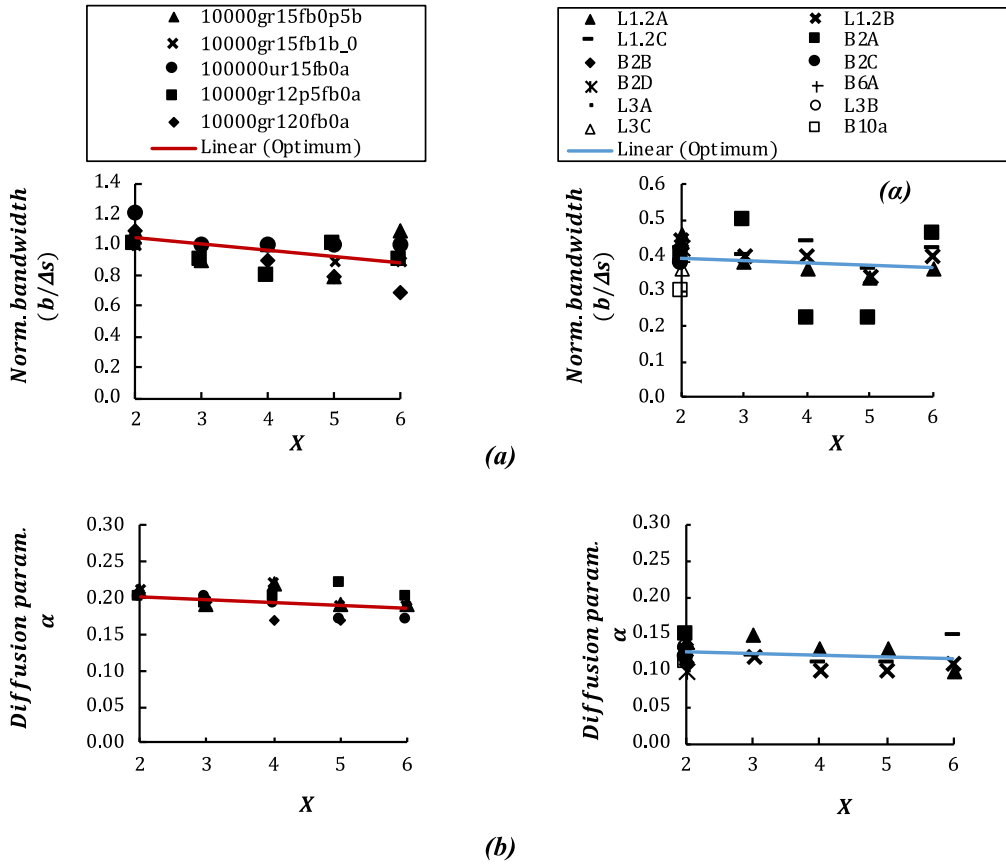


Figure 6. Selection of optimal user-specified parameters in case of the (a) Kernel method (b) Diffusion method, (left) 2D and (right) 3D implementations.

Thus, a trendline is introduced in both plots, as optimum, that describes the relationship between $b/\Delta s$ and X multiplier based on the average values defined in each case. Furthermore, the data suggest that an average normalized bandwidth $(b/\Delta s)_{2D} = 1$ may be used across a range of 2D samples and a bandwidth $(b/\Delta s)_{3D} = 0.4$ may be used across a range of 3D samples without severely compromising the method's accuracy.

Applying the same logic to *Diffusion* method, porosity of every sample was initially estimated for several values of the smearing parameter, α , ranging from 0.01 to 0.3. Then the parameter α that revealed the minimum error for each studied case was plotted against the multiplier X . Referring to **Figure 6b**, the data accumulate around specific values of α for both the 2D (*left*) and the 3D (*right*) implementations. Specifically, in case of the 2D samples the average accuracy improves for α values between 0.15 and 0.22 and in case of the 3D samples between 0.10 and 0.15. Finally, it is observed that the selection of a suitable α is not severely affected by the X multiplier, hence $\alpha_{2D} = 0.17$ can be used across the 2D samples and $\alpha_{3D} = 0.12$ can be used across the 3D samples.

DISCUSSION

Having established the parameters and characteristics of each algorithm, a comparison is carried out among the presented methods in terms of error (%), computational cost and smoothness. Sample 10000gr12p5fb0a is selected as the reference sample for the comparison of the 2D CG schemes and sample L1.2a is selected for the 3D CG schemes. For both cases a Eulerian cell size multiplier $X=3$ is assumed. The calibration parameters of the methods are summarized in **Table 4** for the 2D and **Table 5** for the 3D.

Table 4. Summary of the parameters (sample - 10000gr12p5fb0a) used in the comparison of the 2D methods

Kernel method ($b/\Delta s$)	Diffusion based method (α)	Hybrid method (pixel grid)	Voxel method (pixel grid)
1	0.17	50x50	300x300

Table 5. Summary of the parameters (sample – L1.2a) used in the assessment of the 3D methods

Kernel method ($b/\Delta s$)	Diffusion based method (α)	Hybrid method (pixel grid)	Voxel method (pixel grid)
0.4	0.12	20x20x20	50x50x50

A direct comparison among the 2D methods is presented in the bar chart of **Figure 7a**. The *PCM* is found the least accurate (approximately 17% error) and the *Hybrid* (approximately 0.3% error) together with the *Analytical* the most accurate methods. The *Diffusion* based method manages to increase the *PCM* accuracy by almost 3 times, giving an error of 6.1%, while the *Kernel* method performed even better reporting 3.8% error. The *Voxel* method is ranked fourth in terms of accuracy, presenting 8.8% error. Likewise, the computational cost varies significantly amongst the implemented methods. The most cost-efficient ones are the *PCM* and *Analytical*, while the *Voxel* method is over 3,000 times more computationally demanding. The *Diffusion* based method is 3 times slower and both the *Hybrid* and the *Kernel* 26 times slower than the *PCM*. Regarding the smoothness metric *PCM* demonstrates the highest gradients (worst case) and the *Kernel* method the lowest (best case). The *Analytical* and *Hybrid* methods show comparable smoothness values which are 70% reduced compared with the *PCM*. The *Diffusion* method is the second-best method in terms of this metric, reducing the *PCM* average gradient to more than half.

The comparison among the 3D algorithms is illustrated in **Figure 7b**. The *Voxel* method yielded the highest error, approximately 8%, which is attributed to the low resolution that was selected. In contrast, the *Hybrid* method displays the greatest accuracy, only 1.4% error, while the performance of the *Kernel* and *Diffusion* methods is again remarkable displaying 1.7% and 2.5% errors respectively. In terms of computational time the *Voxel* method is again the most demanding, requiring almost 7,000 times more computational time compared to the *PCM* and *Analytical* method. The *Hybrid* method is the second most demanding, cost wise, however is

still two orders of magnitude faster compared to the *Voxel*. All methods managed to reduce the high gradients observed at the *PCM* smoothness tests, with the *Kernel* method to be proven the most appealing as an average reduction of 76% is attained.

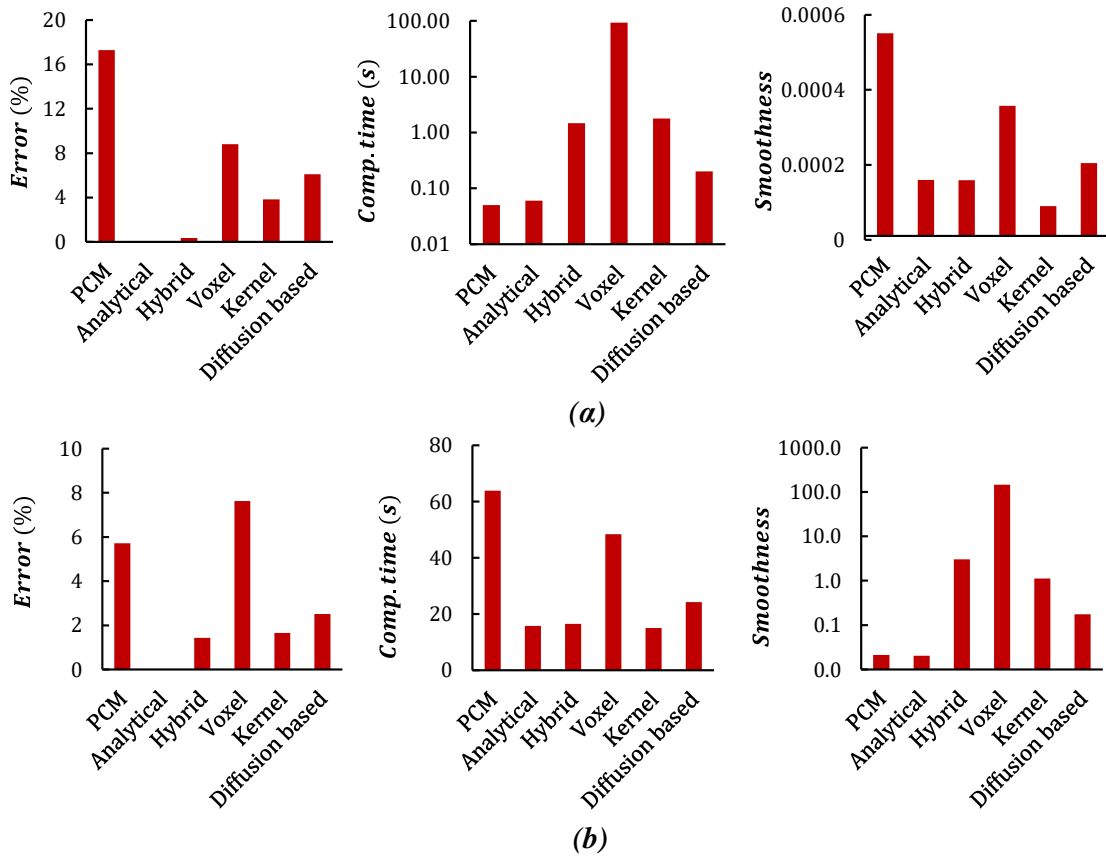


Figure 7. Illustration of the Error (%), computational time (s), smoothness of each method when applied to (a) the 2D sample 10000gr12p5fb0a (b) the 3D sample L1.2a.

CONCLUSIONS

In this study, six different porosity CG schemes were reviewed and applied to 2D and 3D systems of circular / spherical particles with periodic boundaries. This work was motivated by the inability of the most commonly used Particle centroid Method to accurately reproduce the required CG of porosity and similar fields. The schemes studied were *PCM* an *Analytical method*, a *Kernel based method*, a *Diffusion based method*, together with two novel methods called the *Voxel* and *Hybrid methods*. The optimal user-defined parameters needed to apply the methods were selected by considering “accuracy”, “smoothness” and “computational cost” based on available two and three-dimensional DEM-CFD samples.

In conclusion, it was shown that the *Kernel* and *Diffusion based* methods required calibration in terms of the kernel width and diffusion magnitude, before any further evaluation is conducted, but once tuned they can provide cost-effective and reasonable representations of coarse-grained fields for the studied samples. The proposed *Voxel* and *Hybrid* methods showed high accuracy, giving the user control over accuracy against computational cost, an advantage that is not included in any other method found in Literature. The main drawback identified is the high computational resources required in case of the *Voxel* method, especially when 3D implementations are assessed. A wider range of samples could be examined in order to confirm a universal validity of the suggested parameters. All studied schemes demonstrated a more accurate depiction of the calculated fields compared to the *PCM* with varying degrees of smoothness and ease of implementation in CFD solvers.

REFERENCES

- Bnà, S., Manservigi, S., Scardovelli, R., Yecko, P., & Zaleski, S. (2015). Numerical integration of implicit functions for the initialization of the VOF function. *Computers & Fluids*, *113*, 42–52. <https://doi.org/10.1016/j.compfluid.2014.04.010>
- Boyce, C. M., Holland, D. J., Scott, S. A., & Dennis, J. S. (2014). Novel fluid grid and voidage calculation techniques for a discrete element model of a 3D cylindrical fluidized bed. *Computers & Chemical Engineering*, *65*, 18–27. <https://doi.org/10.1016/j.compchemeng.2014.02.019>
- Bullock, Z., Dashti, S., Liel, A. B., Porter, K. A., & Karimi, Z. (2019). Assessment Supporting the Use of Outcropping Rock Evolutionary Intensity Measures for Prediction of Liquefaction Consequences. *Earthquake Spectra*, *35*(4), 1899–1926. <https://doi.org/10.1193/041618EQS094M>
- Clarke, D. A., Sederman, A. J., Gladden, L. F., & Holland, D. J. (2018). Investigation of Void Fraction Schemes for Use with CFD-DEM Simulations of Fluidized Beds. *Industrial & Engineering Chemistry Research*, *57*(8), 3002–3013. <https://doi.org/10.1021/acs.iecr.7b04638>
- Darmana, D., Deen, N. G., & Kuipers, J. A. M. (2005). Detailed modeling of hydrodynamics, mass transfer and chemical reactions in a bubble column using a discrete bubble model. *Chemical Engineering Science*, *60*(12), 3383–3404. <https://doi.org/10.1016/j.ces.2005.01.025>
- Fitzgerald, B. W., Zarghami, A., Mahajan, V. V., Sanjeevi, S. K. P., Mema, I., Verma, V., El Hasadi, Y. M. F., & Padding, J. T. (2019). Multiscale simulation of elongated particles in fluidised beds. *Chemical Engineering Science: X*, *2*, 100019. <https://doi.org/https://doi.org/10.1016/j.cesx.2019.100019>
- Forcellini, D. (2020). Soil-structure interaction analyses of shallow-founded structures on a potential-liquefiable soil deposit. *Soil Dynamics and Earthquake Engineering*, *133*, 106108. <https://doi.org/https://doi.org/10.1016/j.soildyn.2020.106108>
- Foster, M., Fell, R., & Spannagle, M. (2000). The statistics of embankment dam failures and accidents. *Canadian Geotechnical Journal*, *37*(5), 1000–1024. <https://doi.org/10.1139/t00-030>
- Freireich, B., Kodam, M., & Wassgren, C. (2010). An exact method for determining local solid fractions in discrete element method simulations. *AIChE Journal*, *56*(12), 3036–3048. <https://doi.org/10.1002/aic.12223>
- Glasser, B. J., & Goldhirsch, I. (2001). Scale dependence, correlations, and fluctuations of stresses in rapid granular flows. *Physics of Fluids*, *13*(2), 407–420. <https://doi.org/10.1063/1.1338543>
- Goldhirsch, I. (2010). Stress, stress asymmetry and couple stress: from discrete particles to continuous fields. *Granular Matter*, *12*(3), 239–252. <https://doi.org/10.1007/s10035-010-0181-z>
- Hoomans, B. P. B., Kuipers, J. A. M., Briels, W. J., & van Swaaij, W. P. M. (1996). Discrete particle simulation of bubble and slug formation in a two-dimensional gas-fluidised bed: A hard-sphere approach. *Chemical Engineering Science*, *51*(1), 99–118. [https://doi.org/10.1016/0009-2509\(95\)00271-5](https://doi.org/10.1016/0009-2509(95)00271-5)
- Imole, O. I., Krijgsman, D., Weinhart, T., Magnanimo, V., Chávez Montes, B. E., Ramaioli, M., & Luding, S. (2016). Reprint of “Experiments and discrete element simulation of the dosing of cohesive powders in a simplified geometry.” *Powder Technology*, *293*, 69–81. <https://doi.org/10.1016/j.powtec.2015.07.052>
- Itasca Consulting Group Inc. (2008). *Particle Flow Code in 3 Dimensions CCFD Add-on*.
- Jing, L., Kwok, C. Y., Leung, Y. F., & Sobral, Y. D. (2016). Extended CFD-DEM for free-surface flow with multi-size granules. *International Journal for Numerical and Analytical Methods in Geomechanics*, *40*(1), 62–79. <https://doi.org/10.1002/nag.2387>
- Kalderon, M. (2017). A Fundamental Assessment of Computational Porosity. *M.Sc. Thesis, Imperial College London*. <https://doi.org/10.5281/zenodo.4436747>
- Kalderon, M., Smith, E., & O’Sullivan, C. (2021). Comparative analysis of porosity coarse-graining techniques for discrete element simulations of dense particulate systems. *Computational Particle Mechanics*. <https://doi.org/10.1007/s40571-021-00402-4>
- Kawaguchi, T., Sakamoto, M., Tanaka, T., & Tsuji, Y. (2000). Quasi-three-dimensional numerical simulation of spouted beds in cylinder. *Powder Technology*, *109*(1), 3–12. [https://doi.org/10.1016/S0032-5910\(99\)00222-3](https://doi.org/10.1016/S0032-5910(99)00222-3)
- Khawaja, H. A., Scott, S. A., Virk, M. S., & Moatamedi, M. (2012). Quantitative Analysis of Accuracy of Voidage Computations in CFD-DEM Simulations. *The Journal of Computational Multiphase Flows*, *4*(2), 183–192. <https://doi.org/10.1260/1757-482X.4.2.183>
- Kloss, C., Goniva, C., Hager, A., Amberger, S., & Pirker, S. (2012). Models, algorithms and validation for opensource DEM and CFD-DEM. *Progress in Computational Fluid Dynamics*, *12*, 140–152.

<https://doi.org/10.1504/PCFD.2012.047457>

- Link, J. M., Cuypers, L. A., Deen, N. G., & Kuipers, J. A. M. (2005). Flow regimes in a spout–fluid bed: A combined experimental and simulation study. *Chemical Engineering Science*, *60*(13), 3425–3442. <https://doi.org/10.1016/j.ces.2005.01.027>
- Lopez-Caballero, F., & Modaressi-Farahmand-Razavi, A. (2013). Numerical simulation of mitigation of liquefaction seismic risk by preloading and its effects on the performance of structures. *Soil Dynamics and Earthquake Engineering*, *49*, 27–38. <https://doi.org/https://doi.org/10.1016/j.soildyn.2013.02.008>
- MATLAB. (2010). *version 7.10.0 (R2010a)* (version 7.10.0 (R2010a)). The MathWorks Inc.
- Mema, I., Mahajan, V. V., Fitzgerald, B. W., & Padding, J. T. (2019). Effect of lift force and hydrodynamic torque on fluidisation of non-spherical particles. *Chemical Engineering Science*, *195*, 642–656. <https://doi.org/10.1016/j.ces.2018.10.009>
- O’Sullivan, C. (2011). *Particulate Discrete Element Modelling: A Geomechanics Perspective* (1st ed.). CRC Press. <https://doi.org/10.1201/9781482266498>
- Peng, Z., Moghtaderi, B., & Doroodchi, E. (2016). A modified direct method for void fraction calculation in CFD–DEM simulations. *Advanced Powder Technology*, *27*(1), 19–32. <https://doi.org/10.1016/j.apt.2015.10.021>
- Plimpton, S. (1995). Fast Parallel Algorithms for Short-Range Molecular Dynamics. *Journal of Computational Physics*, *117*(1), 1–19. <https://doi.org/10.1006/JCPH.1995.1039>
- Richards, W. A. (1995). The common content of a sphere and a regular tetrahedron having a common centre. *International Journal of Mathematical Education in Science and Technology*, *26*(2), 257–266. <https://doi.org/10.1080/0020739950260211>
- Roy, S., Scheper, B. J., Polman, H., Thornton, A. R., Tunuguntla, D. R., Luding, S., & Weinhart, T. (2019). Surface flow profiles for dry and wet granular materials by Particle Tracking Velocimetry; the effect of wall roughness. *The European Physical Journal E*, *42*(2), 14. <https://doi.org/10.1140/epje/i2019-11778-x>
- Shire, T. (2014). *Micro-scale modelling of granular filters* [PhD Thesis, Imperial College London]. <http://hdl.handle.net/10044/1/12967>
- Strobl, S., Formella, A., & Pöschel, T. (2016). Exact calculation of the overlap volume of spheres and mesh elements. *Journal of Computational Physics*, *311*, 158–172. <https://doi.org/10.1016/j.jcp.2016.02.003>
- Summersgill, F. (2009). *The use of particulate discrete element modelling to assess the vulnerability of soils to suffusion*. M.Eng Thesis, Imperial College London.
- Sun, R., & Xiao, H. (2015a). Diffusion-based coarse graining in hybrid continuum–discrete solvers: Theoretical formulation and a priori tests. *International Journal of Multiphase Flow*, *77*, 142–157. <https://doi.org/10.1016/j.ijmultiphaseflow.2015.08.014>
- Sun, R., & Xiao, H. (2015b). Diffusion-based coarse graining in hybrid continuum–discrete solvers: Applications in CFD–DEM. *International Journal of Multiphase Flow*, *72*, 233–247. <https://doi.org/10.1016/j.ijmultiphaseflow.2015.02.014>
- Tomiya, A., Žun, I., Higaki, H., Makino, Y., & Sakaguchi, T. (1997). A three-dimensional particle tracking method for bubbly flow simulation. *Nuclear Engineering and Design*, *175*(1–2), 77–86. [https://doi.org/10.1016/S0029-5493\(97\)00164-7](https://doi.org/10.1016/S0029-5493(97)00164-7)
- Tsuji, Y., Kawaguchi, T., & Tanaka, T. (1993). Discrete particle simulation of two-dimensional fluidized bed. *Powder Technology*, *77*(1), 79–87. [https://doi.org/10.1016/0032-5910\(93\)85010-7](https://doi.org/10.1016/0032-5910(93)85010-7)
- Wu, C. L., Zhan, J. M., Li, Y. S., Lam, K. S., & Berrouk, A. S. (2009). Accurate void fraction calculation for three-dimensional discrete particle model on unstructured mesh. *Chemical Engineering Science*, *64*(6), 1260–1266. <https://doi.org/10.1016/j.ces.2008.11.014>
- Xiao, H., & Sun, J. (2011). Algorithms in a Robust Hybrid CFD-DEM Solver for Particle-Laden Flows. *Communications in Computational Physics*, *9*(02), 297–323. <https://doi.org/10.4208/cicp.260509.230210a>
- Xue, X., & Yang, X. (2014). Seismic liquefaction potential assessed by fuzzy comprehensive evaluation method. *Natural Hazards*, *71*(3), 2101–2112. <https://doi.org/10.1007/s11069-013-0997-z>
- Zhu, H. P., & Yu, A. B. (2002). Averaging method of granular materials. *Physical Review E*, *66*(2), 021302. <https://doi.org/10.1103/PhysRevE.66.021302>